Journal of ELECTRONIC MATERIALS, Vol. 48, No. 2, 2019
https://doi.org/10.1007/s11664-018-6768-6

Effect of Zinc Addition on the Microstructure, Thermal and Mechanical Properties of Indium-Tin-*x*Zinc Alloys

JINGZE WANG,[1,2] DONGXIN MAO,[1] LEI SHI,[1] WEI ZHANG,[1] and XIAOHUA ZHANG[1]

1.—School of Materials Science and Engineering, Harbin University of Science and Technology, Harbin 150040, China. 2.—e-mail: wangjingze310@163.com

The effect of different Zn content on the microstructure, thermal and mechanical properties of In-Sn-*x*Zn alloys was investigated. The microstructure of the alloys was analyzed by optical microscopy, x-ray diffraction, transmission electron microscopy, scanning electron microscopy and energy dispersive spectroscopy. The results indicated that the alloys consisted of β, γ and Zn phases. The γ phase was generated from the decomposed supersaturation β phase in the peritectic structure, with less than 2.0 wt.% Zn content, characterized by a 120°C phase transition temperature. And a close mutual lattice relation was maintained between β and γ phases. The alloys, with Zn content from 3.0 wt.% to 6.0 wt.% and a melting point at 108°C, had an eutectic structure. Studies indicated that the morphology and distribution of the Zn phases were significantly affected by the β phase. The primary Zn tended to grow along the vertical crystal orientations and to form a cube-shaped block in the β phase. Other Zn existed in the form of a precipitate particle phase in the β phase. Most of Zn was excluded from the γ phase region, which had an effect on the phase boundary of β/γ. And the phase relationship between γ and β in In-Sn-4Zn is $[01\bar{1}]_\gamma//[\bar{1}21]_\beta$,$(111)_\gamma//(210)_\beta$. The performance of the material was significantly enhanced by Zn. When Zn content was 6.0 wt.%, microhardness and elongation of the material were increased by about 160% and 100% respectively, compared with those of In-49Sn-1Zn. Under coupling of the melting interval and the hard phase, the wetting performance of the alloy decreased as the Zn content increased. And the increase of Zn content in the solder made the diffusion distance of Cu longer, which promoted the growth of intermetallic compound (IMC).

Key words: In-Sn-Zn, microstructure, thermal properties, mechanical properties

INTRODUCTION

In the field of microelectro-mechanical systems (MEMS), the low-melting-point solders, such as pure indium (In), indium-tin (In-Sn), indium-tin-bismuth (In-Sn-Bi) and indium-tin-zinc (In-Sn-Zn), were applied in the fabrication and packaging of microoptical-electro-mechanical systems (MOEMS), due to their excellent heat and electrical conductivity.[1–5] The In-48Sn eutectic alloy has been applied in the MOEMS field with great potential for its long fatigue life and great ductility, compared with other solder alloys.[6–12] It is also applied for its low melting point, which is known as 120°C. However, problems such as mechanical fatigue, thermal fatigue and electromigration still threaten the life of the In-48Sn and accelerate the failure of the solder. Some related studies are as follows. Koo and Jung et al.[6–9] studied the formation and growth of intermetallic compounds (IMCs) between In and Sn, such as the β

(Received January 11, 2018; accepted October 27, 2018; published online November 8, 2018)

phase (In_3Sn) and γ phase ($InSn_4$), which were characterized by tetragonal crystal and hexagonal structure, respectively. Their observation was focused on the interfacial reactions and growth kinetics of IMC layers formed at the In-48Sn eutectic solder and bare Au/Cu/Ni. Li et al.[13,14] investigated the electromigration of Cu/In-48Sn/Cu solder bump interconnects. They found that the segregation of the Sn-rich phase and the In-rich phase occurred. An Sn-rich layer and an In-rich layer were formed at the anode and the cathode, respectively. They also studied the thickness of the cathode IMC and anode IMC with increasing electromigration time. Nevertheless, the performance and solidification characteristics of the solder alloys have not been studied in detail. The melting point of the In-46Sn-2Zn eutectic alloy is 107°C, which is lower than that of the industry-recommended In-48Sn solder. So, the Sn-In-Zn near-eutectic solder still maintains a lower melting point. For that, the Sn-In-Zn ternary alloys are also favored in the MOEMS field.[15–20] As a kind of solder, minor In-46Sn-2Zn eutectic structure may weaken the reliability of the solder joints. McCormack et al.[21] found and discussed the disadvantage of In-46Sn-2Zn eutectic structure. Nevertheless, with the adoption of the liquid metal, the alloys with low melting point are coming to play an increasingly important role in the development of emerging technology fields.[22–24] Furthermore, Zn has received much attention in regard to study of In-Sn base alloys for its cheapness and effectiveness as an additive, which may be why it improves the performance of the alloy matrix. In view of this method, Lin and Chang et al.[15,16] have done a lot of research on the interfacial reactions between Sn-20In-*x*Zn solders and Cu at different temperatures. It was found that the reaction phase formation and interfacial morphologies are strongly influenced by Zn concentrations. Perhaps a similar effect will also appear when Zn is added into the In-Sn near-eutectic alloy. Although the research on Zn as an alloy element added into tin (Sn), indium (In) and indium-tin (In-Sn) base alloys has been widely reported,[15–19] the alloying mechanism hasn't been studied systematically. In particular, the IMCs with unique structures and properties, In_3Sn and $InSn_4$, formed in an In-Sn binary system, will significantly change the properties of the matrix by Zn. The alloying process of Zn in them may be more complex. Therefore, the systematic study of the interaction between Zn and the IMCs will be an indispensable work for understanding and exploring complex functional alloys. At present, In-Sn eutectic alloy has shown a commercial value in the relevant field. With the study of the eutectic region, it is possible to further improve the performance of the material.

In this paper, different contents of Zn (1.0–6.0 wt.%) were added into the In-Sn near-eutectic alloys. The effect of Zn on the solidification characteristic and mechanical properties of the alloys were investigated. And detailed analysis of the formation mechanism of different Zn phase was performed, combined with the microstructures of the alloys.

MATERIALS AND EXPERIMENTS

The In-(50 − *x*)Sn-*x*Zn (*x* = 1.0, 2.0, 3.0, 4.0, 5.0, and 6.0) alloys were fabricated using pure In (99.99 wt.%), pure Sn (99.99 wt.%) and pure Zn (99.99 wt.%). The mixed components were encapsulated in quartz tubes with the protection of reductive rosin for preventing oxidation, and then melted by high-frequency induction heating equipment at 500°C for 2) for homogenization. The alloys, solidified to Φ8 × 40-mm cylindrical ingots (Φ was the diameter of the cylindrical ingots), were rolled into 0.3-mm-thick ingots along the same direction at room temperature.

For differential scanning calorimetry (DSC), a PerkinElmer Diamond DSC instrument was employed, and experiments were carried out over the temperature range from 40°C to 300°C at a scanning rate 10°C/min in a nitrogen atmosphere for preventing oxidation. DUH-211S ultra-micro dynamic hardness measurement was used to measure the microhardness of the series. The experimental force was 10 gf and the loading time was 15 s. The ultimate tensile strength (UTS) and elongation of the alloys were determined using an AGS-J 10KN universal testing machine at room temperature. Every specimen dimension was 40 mm × 3 mm × 0.3 mm, the gauge length was 20 mm and the tensile rate was 6 mm/min. The wetting test was carried out at 200°C using a contact angle measuring instrument. The size of the sample was 3 mm × 3 mm × 2 mm, the substrate was an FR4-type copper-clad substrate and the flux was an AMTECH-4300 flux (USA). The microstructure of the alloys was observed using a GX71-6230 digital optical microscope (OM). The interface morphology of the phases and the phase relationship were determined by transmission electron microscopy (TEM). The phase morphology was identified using a SU8020 scanning electron microscope equipped with attachments for energy dispersive spectroscopy (EDS). An X'PERT Pro MPD diffractometer was utilized for x-ray diffraction (XRD) analysis to determine the phase composition of the alloys.

RESULTS AND DISCUSSION

The Effect of Zn on the Solidification Characteristics of In-Sn-*x*Zn Alloys

Zn as a considerable alloying element is usually added to the low-melting-point alloys based on In-Sn,[15–18] which improves their performance significantly. Because of the low solid solubility of Zn in pure In and Sn, the content of Zn in most commercial alloys is usually no more than 9.0 wt.%. Among them, the eutectic alloys are the most widely used, such as Sn-9Zn,[25–30] due to their relatively

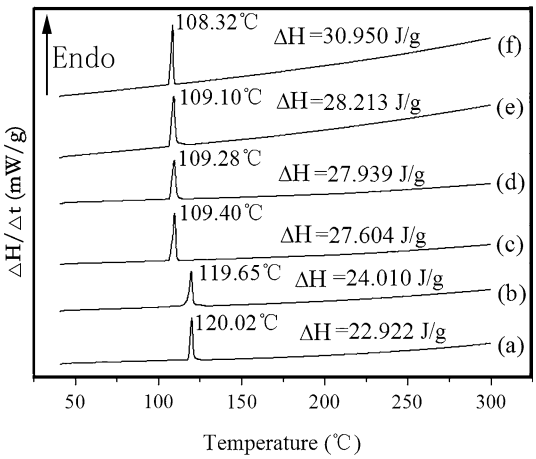

Fig. 1. DSC curves of In-(50 − *x*) Sn-*x*Zn alloys including their melting point and thermal enthalpy (Δ*H*): (a) In-49Sn-1Zn, (b) In-48Sn-2Zn, (c) In-47Sn-3Zn, (d) In-46Sn-4Zn, (e) In-45Sn-5Zn, (f) In-44Sn-6Zn.

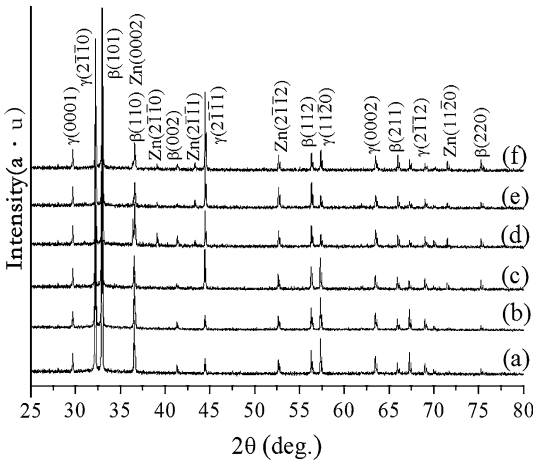

Fig. 2. XRD patterns of the In-(50 − *x*)Sn-*x*Zn alloys including the diffraction peaks of β, γ and Zn phases: (a) In-49Sn-1Zn, (b) In-48Sn-2Zn, (c) In-47Sn-3Zn, (d) In-46Sn-4Zn, (e) In-45Sn-5Zn, (f) In-44Sn-6Zn.

stable solidification characteristics. In In-48Sn eutectic alloy, Lee et al.[10,11] have also reported that there were two types of alloy compounds of In and Sn. These were the β phase (In_3Sn) and γ phase ($InSn_4$), which were characterized by tetragonal crystal and hexagonal structure, respectively. In the Sn-In-Zn system, there was a more complex phase reaction.[31] According to the liquid projections of an Sn-In-Zn ternary system,[32] minor Zn addition (no more than 10 wt.%) may induce three types of phase reactions, which included two types of peritectic reactions, characterized by 179°C and 120°C, respectively, and an eutectic-type reaction, characterized by 107°C. That is,

$$L + (\beta\mathrm{Sn}) \rightarrow (\mathrm{Zn}) + \gamma \quad (1)$$

The reaction temperature is 179°C.

$$L' + (\mathrm{In}) \rightarrow (\mathrm{Zn}) + \beta \quad (2)$$

The reaction temperature is 120°C.

$$L \rightarrow (\mathrm{Zn}) + \gamma + \beta \quad (3)$$

The reaction temperature is 107°C.

The solidification characteristics of In-(50 − *x*)Sn-*x*Zn series were determined by DSC analysis, as shown in Fig. 1. That confirmed the phase reactions above. When the Zn content was 1.0 wt.% and 2.0 wt.%, the melting point of the alloys was near 120°C, which was close to the P2 temperature of In-Sn-Zn system. Nevertheless, when the Zn content was more than 2.0 wt.%, the melting point of the series was near 108°C, which was close to the *E* eutectic temperature of In-Sn-Zn system. The thermal enthalpy (Δ*H*) was increased with increasing Zn content in the alloys. Meanwhile, there were different degrees of upward deviation in the DSC curves (Fig. 1).

According to the results of XRD analysis (Fig. 2), the diffraction characteristics of β and γ phases in the ternary alloys were in agreement with that of the binary eutectic alloy. Based on the reaction temperature of melting characteristics (Fig. 1), it may be determined that the In-49Sn-1Zn and In-48Sn-2Zn were peritectic alloys, and other alloys with 3.0–6.0 wt.% of Zn were eutectic alloys. This suggested that most of Zn, not all, had been precipitated from the β and γ phases during the cooling process. Otherwise, Zn was bound to cause some changes in the lattices of β and γ phases, due to the difference in the atomic size of In, Sn and Zn. Moreover, there was a more significant conflict, which was the eutectic and peritectic alloys were formed at about 108°C and 120°C, respectively, and had almost the same phase compositions. Meanwhile, the initial composition of the peritectic alloys should only contain Zn and β phases, and even perhaps some residual pure In, according to the phase equilibrium formulas.[32]

This conflict could only be explained by the β phase of the peritectic alloys not being stable at lower temperature. With temperature decreasing, it decomposed and generated new β and γ phases. This phase decomposition process could be expressed as follows:

$$\beta' \rightarrow \beta(\mathrm{In_3Sn}) + \gamma + \mathrm{Zn} \quad (4)$$

where it was defined that the supersaturation peritectic β phase was β', that was different from the new β (In_3Sn).

The Effect of Zn on the Microstructure of In-Sn-*x*Zn Alloys

The Identification of Different Phase Characteristics

By EDS analysis, the different phases of the alloys were distinguished obviously (Fig. 3). According to the composition analysis of point A and B, the

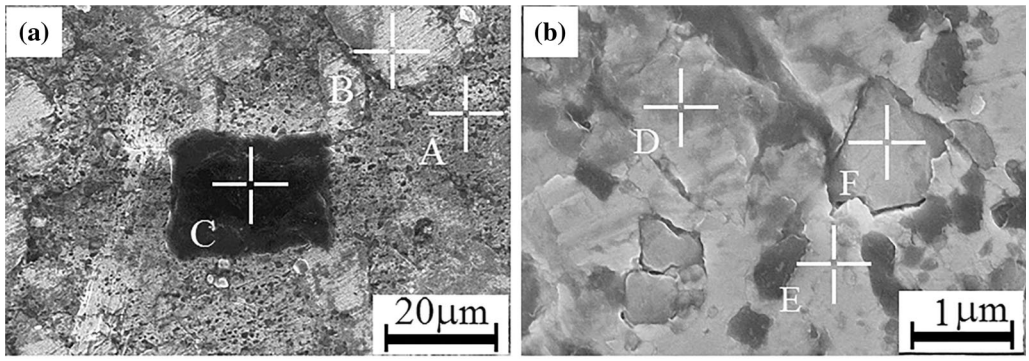

Element	In(At.%)	Sn(At.%)	Zn(At.%)
A	63.60	33.44	02.97
B	25.67	72.52	01.82
C	12.84	03.54	83.62

Element	In(At.%)	Sn(At.%)	Zn(At.%)
D	68.28	28.81	02.91
E	64.07	33.58	02.35
F	14.53	07.21	78.26

Fig. 3. The EDS results of In-47Sn-3Zn eutectic microstructure including the atomic percentage of different points: (a) the atomic percentage on point A, B and C, (b) the atomic percentage of β area (point A) on point D, E and F.

atomic percentage of In and Sn was close to 2:1 and 1:3, respectively. Point C contained a large amount of Zn and a little amount of In. Although this analysis may have a little deviation, it could be determined that point A was consistent with the characteristics of In-rich β phase. Similarly, point B and C were consistent with the Sn-rich γ phase and Zn phase respectively.

By metallographic observation, Zn and γ phases had a homogeneous morphology. Zn phase was black and γ phase was white, and they both embedded in β phase (the gray part in Fig. 3a). Meanwhile, some Zn precipitates were distributed in the β phase diffusely. Point F, according to the Zn particle, was about 1 μm in size. Moreover, there were some differences in composition at different regions of β phase, such as points D and E.

The Formation Mechanism of Zn Phase (Including the Primary and Precipitate Particles)

On OM observation, as shown in Fig. 4, in addition to In-49Sn-1Zn, the block Zn phases existed in other alloys and the number of that increased with Zn content in the alloys. Partial block Zn showed a regular square morphology. A similar morphology was also reported in the In-Sn base alloys.[20,33] Wu et al.[33] found that the formation of regular morphology often appeared in the conventional casting process with a slow solidification rate. Nevertheless, there was a lower possibility of the formation in the continuous casting process. Apparently, the coarse block phases with regular shape may be the primary phases of Zn. Moreover, the melting point of Zn (420°C) was higher than the peritectic point (120°C) and eutectic point (107°C) of the alloys. With temperature decreasing, the primary Zn phase could be fully grown in a wider crystalline region. In this process, the first precipitate phases, to grow faster, usually preferentially grow in the crystal plane and orientation with fewer atoms. Elemental Zn has a closely packed hexagonal structure with lattice constants of a = 244.49 pm and c = 494.68 pm. On the crystal plane $(10\bar{1}0)$ with fewer atoms of pure Zn, the included angle between the crystal orientation $[2\bar{4}2\bar{3}]$ and $[\bar{2}42\bar{3}]$ is 94.27° (Fig. 5b). The primary Zn phase was likely to grow along these two directions. Therefore, the primary Zn phases quickly grew along the near-vertical directions to form a regular morphology.

The other existing form of Zn was a fine precipitate particle in the alloys. By OM observation, the precipitate Zn particles mainly existed in the β phase. The formation of precipitation phases indicated that the β phase had dissolved a lot of Zn at a high temperature. Meanwhile, the solid solubility of Zn in β phase decreased with temperature decreasing. Nevertheless, the solid solubility of Zn in γ phase, by contrast, was much smaller than that in β phase. Therefore, the solubility of Zn in γ phase was affected by temperature insignificantly. This phenomenon may be explained by the EDS results of the Zn particle phase (Fig. 3b). The In content in the Zn particle phase was as high as 14 at.%, while there was little of Sn in it. It may be inferred that there was some composition similarity between the Zn particle phase and β phase. Therefore, the Zn particles were mainly precipitated from β phase with temperature decreasing.

The Formation and Difference of Peritectic and Eutectic Structures of the Alloys

The formation process of the peritectic and eutectic structures in the alloys was also affected by Zn,

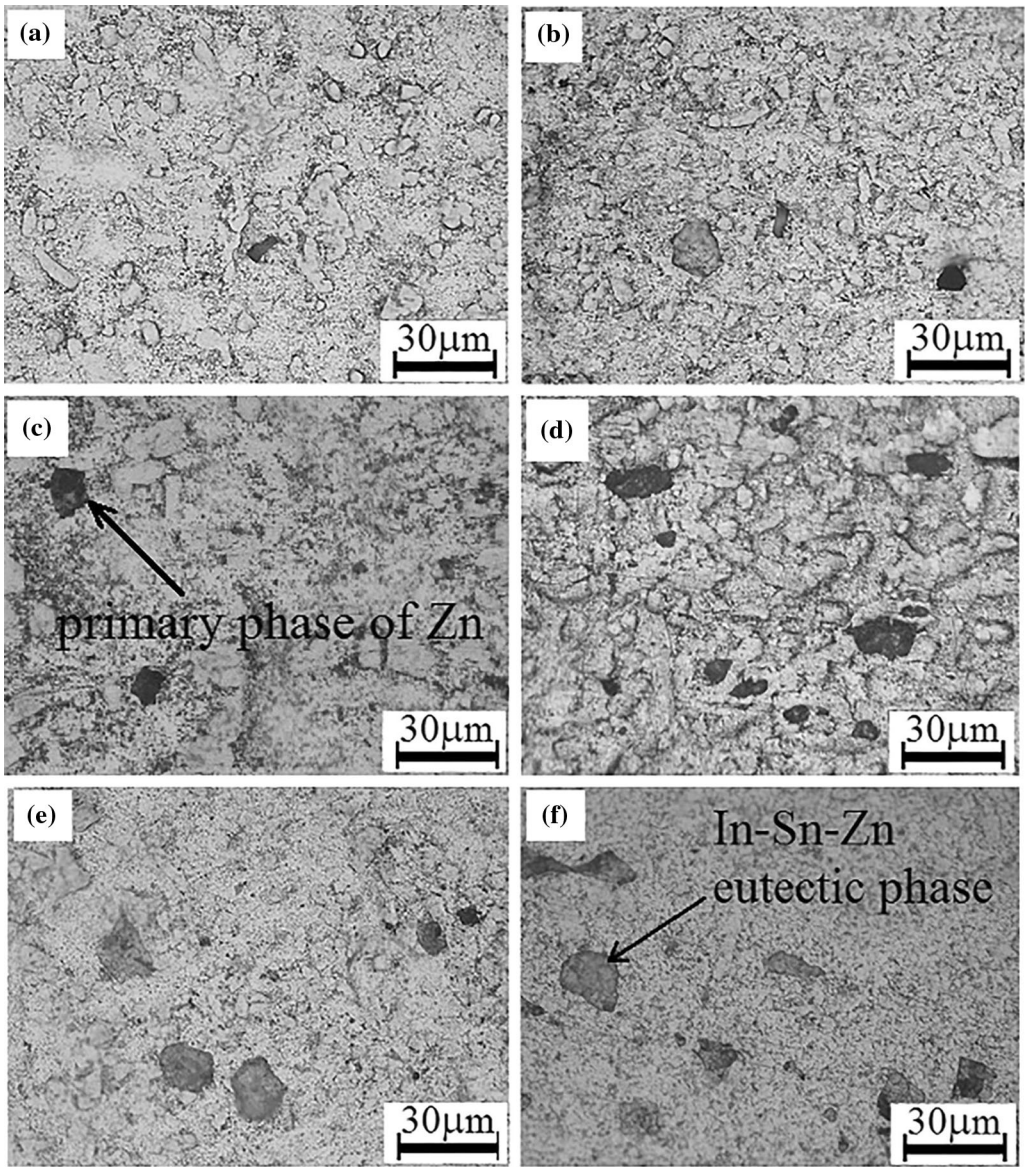

Fig. 4. Optical micrographs of In-(50 − *x*)Sn-*x*Zn alloys including primary Zn phases and In-Sn-Zn eutectic phases: (a) In-49Sn-1Zn, (b) In-48Sn-2Zn, (c) In-47Sn-3Zn, (d) In-46Sn-4Zn, (e) In-45Sn-5Zn, (f) In-44Sn-6Zn.

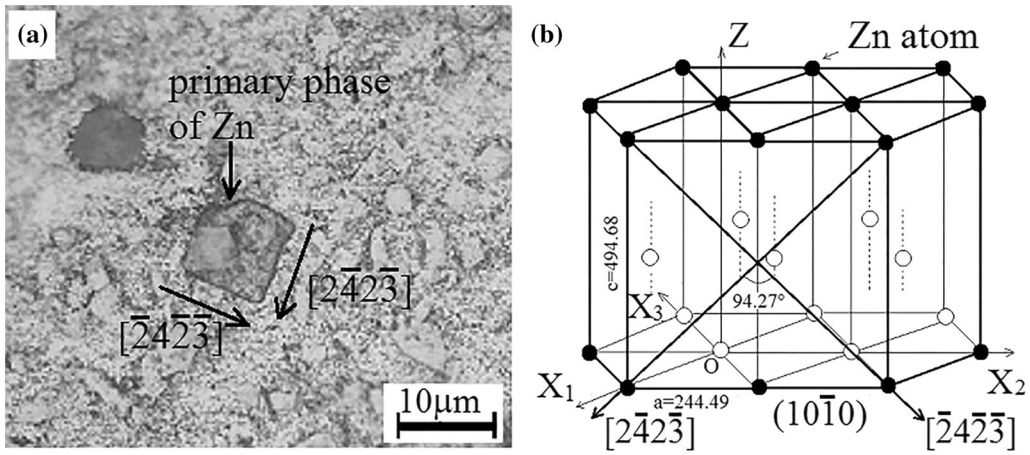

Fig. 5. Formation process of primary Zn phase in In-(50 − *x*)Sn-*x*Zn alloys: (a) the primary Zn phase in the alloys, (b) the growth direction of Zn.

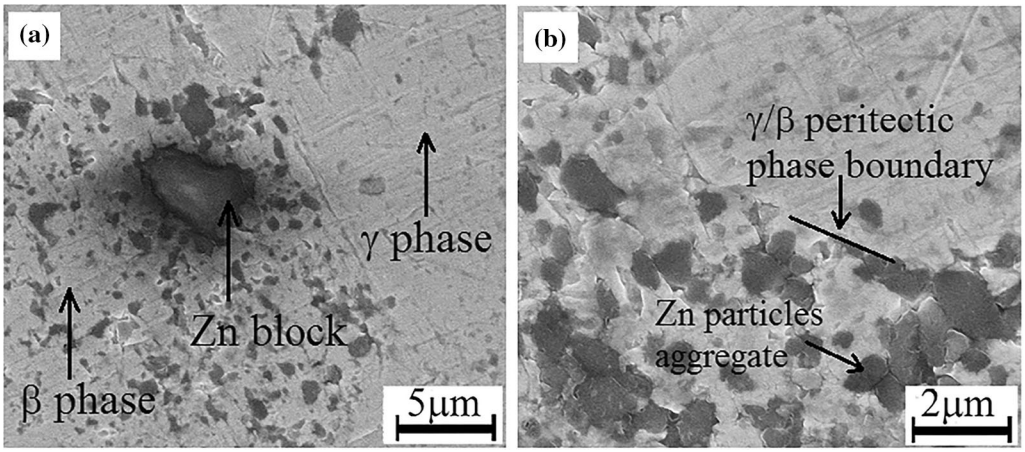

Fig. 6. SEM images of In-49Sn-1Zn alloy: (a) the peritectic structure, (b) Zn particle aggregate and the phase boundary of β and γ phases.

due to the different effects of Zn on the β and γ phases.

By SEM observation of the In-49Sn-1Zn peritectic structure (Fig. 6a), the boundary of β and γ phases implied the formation process of γ phase. There was no obvious boundary between the β and γ phases, while the distribution of the precipitation Zn phases revealed their respective positions (Fig. 6b). The significant difference between the β and γ phases was that there were more particles and block Zn phases in β phase than that in γ phase. The β and γ phases constituted the peritectic structure, and they were generated from the decomposition of supersaturated β' phase. The indistinct boundaries suggested that there was a close mutual lattice relation between them.

Except for the solid phase transition, it was not easy for the two crystal structures, tetragonal for β phase and hexagonal for γ phase, to maintain coherence. With the decomposition, Zn segregation appeared in the long range. During the formation of γ phase, most of Zn was diffused to the residual β phase, and further increased the supersaturation of β' phase. Zn precipitation occurred in the cooling process. As a result, a large number of Zn particles appeared in β phase, and the excess Zn in γ phase diffused to the boundaries. Most of the Zn particles in β and γ phase boundaries gathered to form massive blocks or aggregates.

The In-Sn-Zn eutectic structure has also been reported by McCormack et al.,[21] and there were some typical divorced eutectic structures found in the eutectic region. In this paper, the SEM observation of In-47Sn-3Zn eutectic structure is shown in Fig. 7. The γ phase, embed in the β phase, was coarse in the alloys, and their phase boundary was obvious. Moreover, there were more Zn particle phases in the phase boundaries. The primary and particle phases of Zn in the eutectic structure were bulkier than that in the peritectic structure. This may be associated with a lower eutectic temperature.

Based on the above analysis, there was a close relationship between the crystallization process of Zn and the β phase in the alloys. With the decomposition of β phase in the peritectic structure, the Zn content was also changed, and Zn concentrated in the residual β phase was increased. Therefore, more precipitate Zn particles grew to form blocks or aggregates. The phase boundaries between β and γ phase were clear and stable. Some precipitation Zn particles dispersed in the β phase. Perhaps, the difference in the microstructures have a great influence on the mechanical properties of the In-Sn-xZn alloys.

To determine a clearer boundary between the two phases, we turned to TEM. The interface morphology of γ and β phases in In-Sn-4Zn was observed by TEM as shown in Fig. 8. By using the Image-Pro software, the maximum distance between the two phase is 58.22 nm and the minimum is 17.07 nm. The phase relationship is calibrated by the electron diffraction spots of γ and β phases, as shown in Fig. 9. The phase relationship between γ and β is $[01\bar{1}]_\gamma // [\bar{1}21]_\beta, (111)_\gamma // (210)_\beta$.

Due to the different solubility of Zn in β and γ phases and the significant effect of temperature on them, there was a strong segregation process of Zn in the formation of peritectic and eutectic structures. This process may hinder the growth of both β and γ phases to form a coarser structure. The dispersion Zn particles are expected to impact the performance of In-Sn-xZn alloys.

The Effect of Zn on the Mechanical Properties of In-Sn-xZn Alloys

Usually, mechanical properties of alloys are characterized by the hardness of materials, especially microhardness. It determines the durability of a material during use and also decides the suitability of the material in certain applications. Microhardness tests typically determine the hardness of total grains and microstructure phases of the alloys.

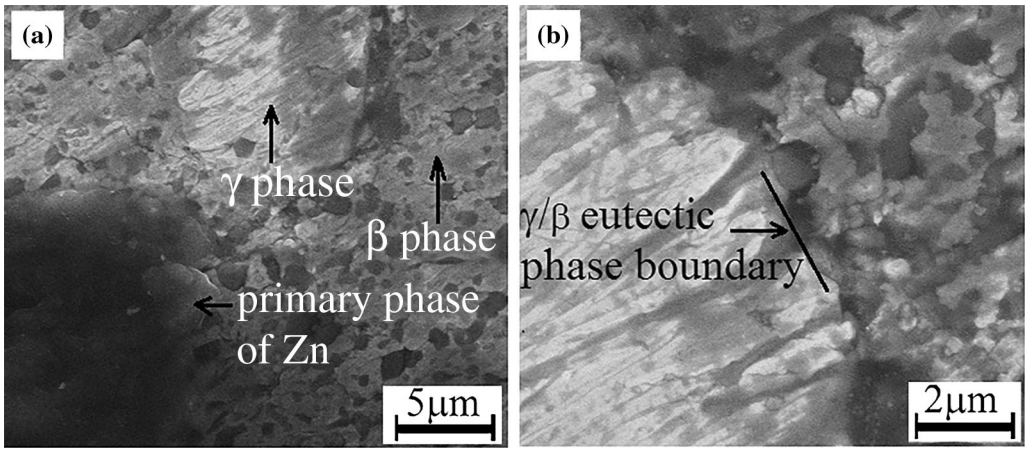

Fig. 7. SEM images of In-47Sn-3Zn alloy: (a) the eutectic structure, (b) the phase boundary of β and γ phases.

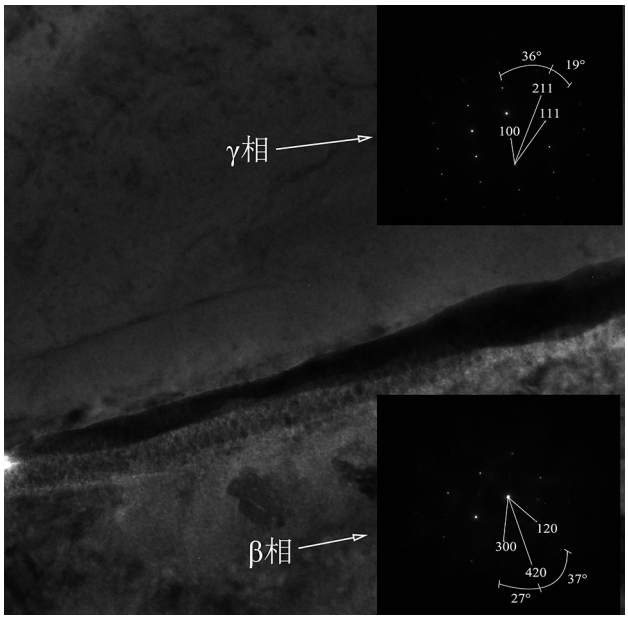

Fig. 8. TEM micrographs of the β/γ phase boundary.

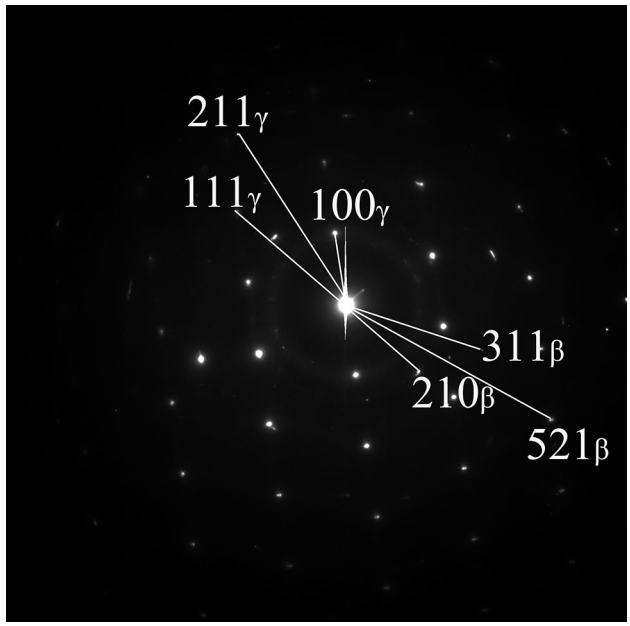

Fig. 9. The synthetic electron diffraction spots of β and γ phases.

Figure 10a shows microhardness values of the Zn-doped In-Sn-*x*Zn alloys. It could be noted that the microhardness value increased as the content of Zn rose from 1.0 wt.% to 6.0 wt.%. Among the In-Sn-*x*Zn(x = 1,2,3,4,5,6) alloys, the maximum microhardness value occurred at 6.0 wt.% Zn (Fig. 10a). Perhaps, due to the refinement of the structure caused by the increase in Zn content, and the presence of a large amount of fine Zn particles in the matrix, especially its dispersion-strengthening effect, the microhardness value is significantly increased.

The tensile strength and plastic deformation of the material can be characterized by the ultimate tensile strength (σ_b) and elongation (δ) respectively. The effect of third element Zn additives on the mechanical properties can be seen from Fig. 10. The elongation (δ) of the alloys was increased as the content of Zn increases from 1.0 wt.% to 6.0 wt.%. The elongation (δ) of In-Sn-1Zn was about 17%, while that of In-Sn-6Zn was up to 30.9% (Fig. 10b). Meanwhile, all of the In-Sn-*x*Zn alloys displayed a typical ductile fracture mode. This indicated that the series had good ductility. From the results, it also can be found that the tensile strength of the material fluctuated from 4 MPa to 6 MPa, and the change is not obvious. This may be due to the fact that the material contains soft β phase.

It can be seen from Fig. 4, when the Zn content was increased to 3 wt.%, the bulky primary Zn phase began to appear in the material. The existence of the bulk primary Zn phase affected the mechanical properties of the material. It was often the place where the crack preferentially expanded, which had a great influence on the tensile properties of the material. And because the number of bulk

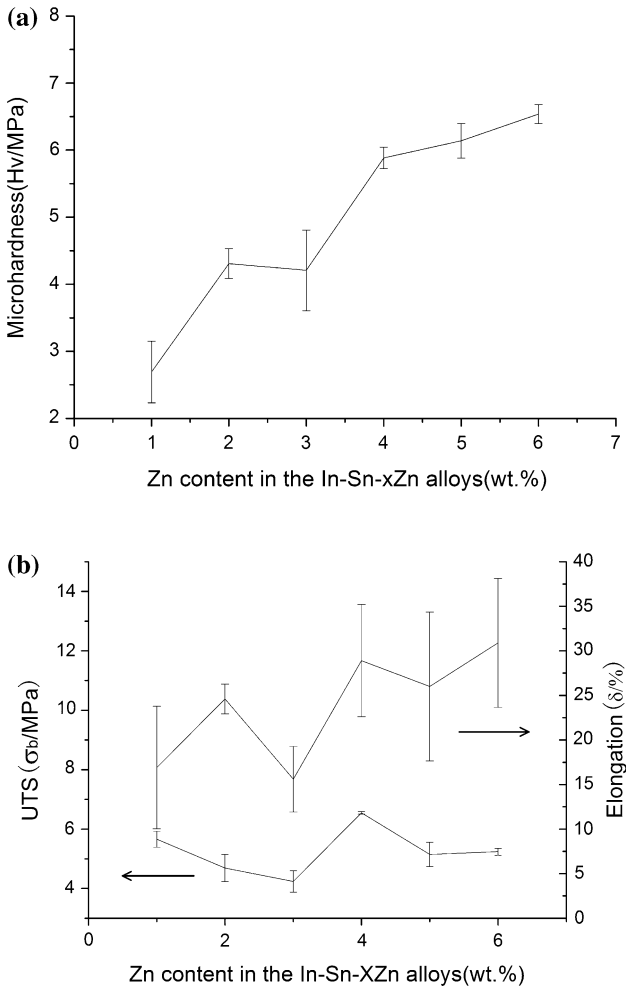

Fig. 10. The mechanical properties of In-Sn-*x*Zn alloys: (a) the microhardness of In-Sn-*x*Zn alloys, (b) the ultimate tensile strength (σ_b) and the elongation (δ) of In-Sn-*x*Zn alloys.

primary Zn phases was small, its effect on microhardness was less pronounced. Therefore, at 3 wt.% Zn content, the microhardness decreased slightly, and the elongation decreased greatly. The increase in Zn content brought about the bulk primary Zn phase, which also significantly increased the amount of dispersed Zn in the matrix. Therefore, although the microhardness and elongation were fluctuating, the overall trend was still rising.

The improvement of mechanical properties was related to the change of the alloy structures caused by Zn. There was an obvious difference in structure and properties between β and γ phases of the alloys. γ phase was much harder than β phase, but was surrounded by β phase. The β phase acted as the matrix, while the γ and Zn phases acted as the reinforcing phase in the alloys. The general view was that the mechanical properties of the alloys were determined by the softer β phase. The strength and plasticity of materials were improved by the refinement of the microstructure, caused by Zn, and the presence of most precipitation Zn particle phases.

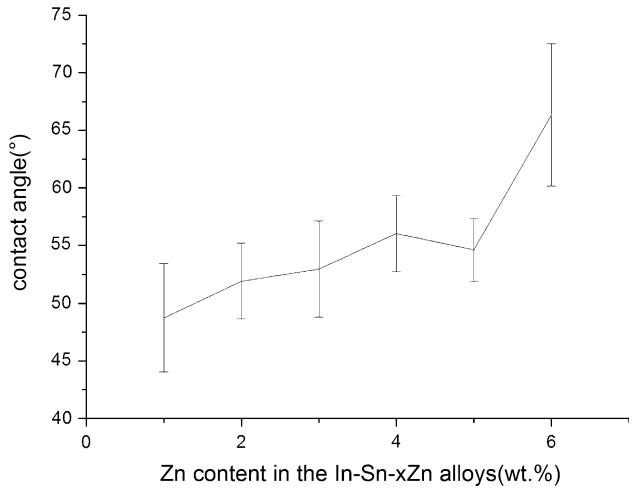

Fig. 11. The contact angle of In-Sn-*x*Zn alloys.

Wettability is one of the important characteristics of In-Sn-*x*Zn alloys. The experimental results are shown in Fig. 11. It can be seen from the figure that the contact angle of the alloy increases with the increase of the Zn content; that is, the wetting performance of the alloy becomes worse and worse.

The wettability of the alloy is related to its melting point and melting interval. The starting point of the absorption peak of the DSC curve is taken as the solidus temperature of the alloy, and the peak of the absorption peak is taken as the liquidus temperature of the alloy. The temperature differential of the two is the melting interval of the material. As shown in Fig. 12, the melting interval of the alloys shows an upward trend, with the exception of the Zn content of 3 wt.% and 6 wt.%. The melting point of the material is shown in Fig. 1. The melting point of the alloy decreased with the addition of Zn. The decrease of the melting point of the material is favorable for improving the wetting performance of the alloy. But eventually, the wettability of the alloy decreased, because the fluidity of the material decreased due to the widening of the alloy's melting interval. Also, from the peak intensity change of XRD (Fig. 1), it can be seen that as Zn increased, the β phase decreased and the γ phase increased. As can be seen from Fig. 4, the primary Zn particles also gradually increased. The increase of these hard phases may cause the material's fluidity to decrease and reduce the wetting properties of the material.

Therefore, under the coupling of the melting interval and the hard phase, the wetting performance of the alloy decreased as the Zn content increased.

The reliability of the solder joint is affected by the atomic diffusion between the solder and the substrate. The diffusion rate of Cu in the solder is the fastest, about 1000 times higher than the diffusion rate of Zn atoms. Therefore, the IMC layer between the solder and the Cu substrate is dominated by the diffusion of Cu atoms. Generally, a thin CuZn layer

is formed on the side close to the Cu substrate, and a Cu_5Zn_8 layer is formed on the side close to the solder.[34] It can be seen from Fig. 13b that the intensity of In and Sn in the IMC layer was close to 0, and the intensity of Cu and Zn was high. Therefore, the IMC layer of the In-Sn-Zn solder should be the compound of Cu and Zn. From the line scan results (Fig. 13), the diffusion distance of Cu was significantly improved with the increase of Zn content. The diffusion distance of Cu in In-45Sn-5Zn was about 11.5 μm, and the diffusion distance in In-49Sn-1Zn was only about 7 μm. Therefore, as shown in Fig. 14, an IMC layer having a thickness of about 15.78 μm appeared in In-45Sn-5Zn. And there was no obvious IMC layer in In-49Sn-1Zn. The IMC layer facilitates metallurgical bonding of the solder to the substrate, but excessive thickness of the IMC layer also reduces solder joint reliability. Therefore, the Zn content in the solder should not be too high.

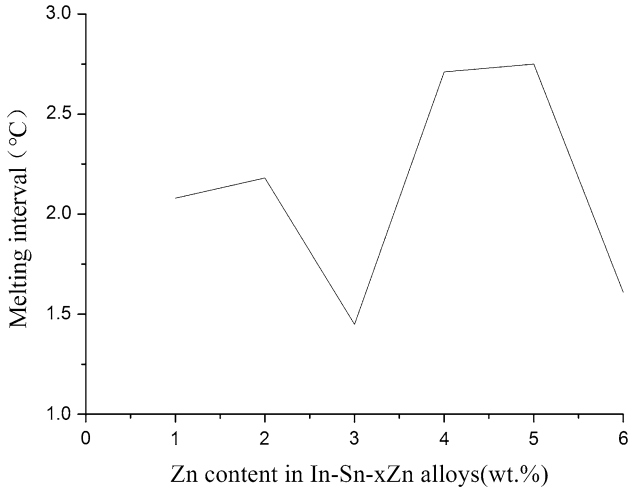

Fig. 12. The melting interval of In-Sn-*x*Zn alloys.

CONCLUSIONS

In this paper, the effects of Zn addition at different amounts (1.0–6.0 wt.%) on the microstructure, thermal and mechanical properties of In-Sn-*x*Zn alloys were investigated. Based on the above analysis, the following conclusions were drawn:

The structure of the series consisted of β, γ and Zn phases. The alloys melted at 120°C, with less than 2.0 wt.% Zn, and had a peritectic structure, in which the γ phase was generated from the decomposed supersaturation β phase. And a close mutual lattice relation was maintained between β and γ phases. The other alloy melted at 108°C, with Zn content from 3.0 wt.% to 6.0 wt.%, and had an eutectic structure with a distinct boundary of β and γ phases. It was conjectured that the morphology and distribution of the Zn phases were significantly affected by β phase. The primary Zn tended to grow along the crystal orientation $[2\bar{4}2\bar{3}]$ and $[\bar{2}42\bar{3}]$ to form a cube-shaped block in β phase in appropriate conditions. Other Zn existed in the form of precipitate particles in β matrix. Due to low solubility, Zn was strongly excluded from γ phase in the process of the β phase decomposition and eutectic matrix. This

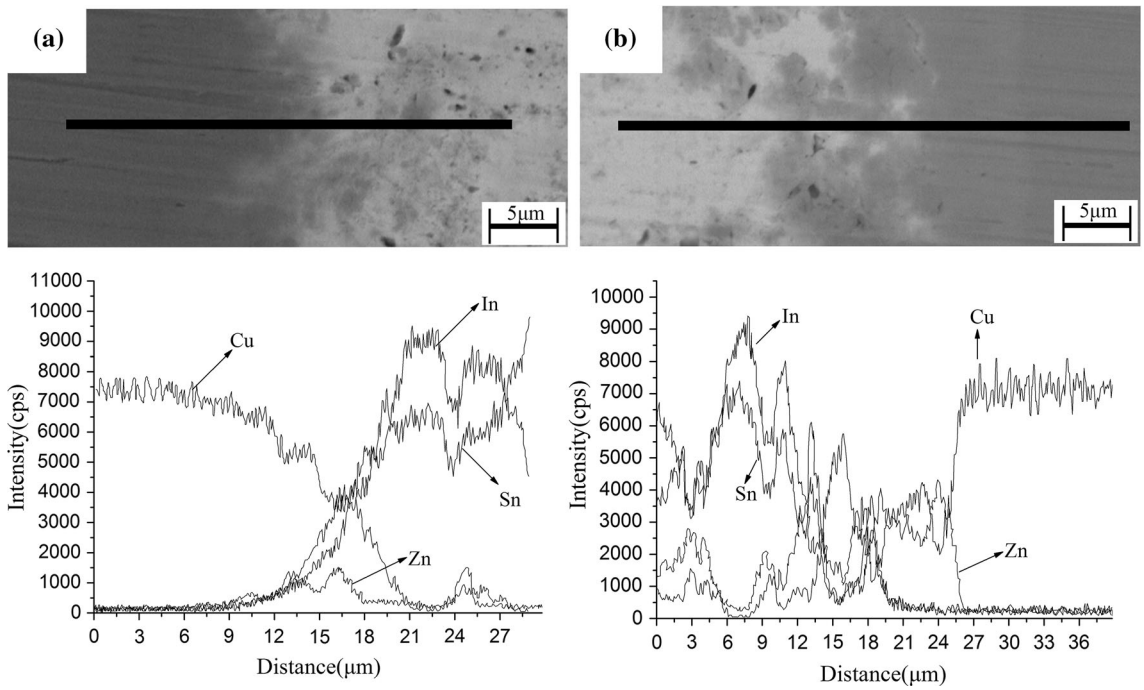

Fig. 13. Line scanning analysis of elements' distribution by EDS in IMC layers of In-(50 − *x*)Sn-*x*Zn alloys: (a) In-49Sn-1Zn, (b) In-45Sn-5Zn.

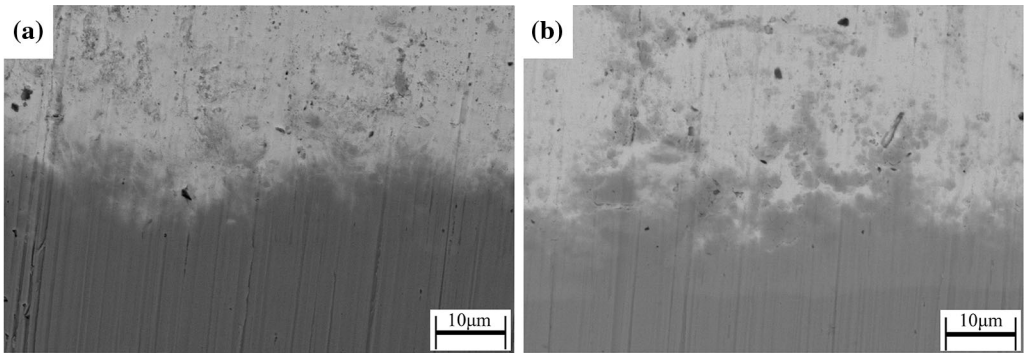

Fig. 14. Back-scattered electron images of the IMC layers between In-(50 − *x*)Sn-*x*Zn alloys and the copper substrate: (a) In-49Sn-1Zn, (b) In-45Sn-5Zn.

increased the uniformity of Zn and resulted in a clear improvement in precipitation effect on β phase. The accumulation of Zn in the boundary of β and γ phases was favorable to the stability of the matrix structure, and the phase relationship between γ and β in In-Sn-4Zn is $[01\bar{1}]_{\gamma}//[\bar{1}21]_{\beta}$,$(111)_{\gamma}//(210)_{\beta}$.

As a result, the performance of the materials was significantly enhanced by Zn. When Zn content reached 6.0 wt.%, the microhardness and elongation of the alloys were increased by nearly 160% and 100%, respectively, compared with those of In-49Sn-1Zn. Under the coupling of the melting interval and the hard phase, the wetting performance of the alloy decreased as the Zn content increased. And the increase of Zn content in the solder made the diffusion distance of Cu longer, which promoted the growth of the IMC.

ACKNOWLEDGMENTS

In this work, the authors would like to thank Professor Pan and Professor Liu at the Center for Material Analysis and Testing, who provided the experimental help. Financial support was provided by the Natural Science Foundation of Heilongjiang Province of the Research E201447 and Science and Technology Research Project of Education Department of Heilongjiang Province of the Research 11521047.

REFERENCES

1. S.W. Chen, C.F. Yang, H.J. Wu, R.B. Chang, and C.M. Hsu, *Mater. Chem. Phys.* 132, 481 (2012).
2. X. Chen, F. Xue, J. Zhou, and Y. Yao, *J. Alloys Compd.* 633, 377 (2015).
3. D.G. Kim and S.B. Jung, *J. Alloys Compd.* 386, 151 (2005).
4. J.W. Kim and S.B. Jung, *Mater. Sci. Eng. A-Struct.* 397, 145 (2005).
5. J.W. Kim and S.B. Jung, *J. Nanosci. Nanotechnol.* 12, 3259 (2012).
6. J.M. Koo and S.B. Jung, *J. Electron. Mater.* 34, 1565 (2005).
7. J.M. Koo and S.B. Jung, *Microsyst. Technol.* 13, 1567 (2007).
8. J.M. Koo, J.W. Yoon, and S.B. Jung, *Surf. Interface Anal.* 38, 426 (2006).
9. J.M. Koo, J.W. Yoon, and S.B. Jung, *J. Mater. Res.* 23, 1631 (2008).
10. K.O. Lee, J.W. Morris, and F. Hua, *J. Electron. Mater.* 41, 336 (2012).
11. K.O. Lee, J.W. Morris, and F. Hua, *J. Electron. Mater.* 42, 168 (2013).
12. S.Y. Li, D.H. Yang, Q. Tan, and L.L. Li, *J. Electron. Mater.* 44, 2007 (2015).
13. Y. Li, A.B.Y. Lim, K.M. Luo, Z. Chen, F.S. Wu, and Y.C. Chan, *J. Alloys Compd.* 673, 372 (2016).
14. Y. Li, F.S. Wu, and Y.C. Chan, *J. Mater. Sci. Mater. Electron.* 26, 8522 (2015).
15. S.K. Lin, R.B. Chang, S.W. Chen, M.Y. Tsai, and C.M. Hsu, *J. Mater. Sci.* 49, 3805 (2014).
16. S.K. Lin, R.B. Chang, S.W. Chen, M.Y. Tsai, and C.M. Hsu, *Mater. Chem. Phys.* 154, 60 (2015).
17. J. Pstrus, *Appl. Surf. Sci.* 265, 50 (2013).
18. M. Rechchach, A. Sabbar, H. Flandorfer, and H. Ipser, *Thermochim. Acta* 502, 66 (2010).
19. D.P. Tao, *J. Alloys Compd.* 457, 124 (2008).
20. H.M. Wu, F.C. Wu, and T.H. Chuang, *J. Electron. Mater.* 34, 1385 (2005).
21. M. McCormack, S. Jin, H.S. Chen, and D.A. Machusak, *J. Electron. Mater.* 23, 687 (1994).
22. M.D. Dickey, *ACS Appl. Mater. Int.* 6, 18369 (2014).
23. R.C. Ma, C.R. Guo, Y.X. Zhou, and J. Liu, *J. Electron. Mater.* 43, 4255 (2014).
24. X.H. Yang, S.C. Tan, B. Yuan, and J. Liu, *Sci. China Technol. Sci.* 59, 597 (2016).
25. S.C. Chang, S.C. Lin, and K.C. Hsieh, *J. Electron. Mater.* 35, 399 (2006).
26. M. Date, T. Shoji, M. Fujiyoshi, K. Sato, and K.N. Tu, *Scr. Mater.* 51, 641 (2004).
27. R.J. Hooper, D.P. Adams, D. Hirschfeld, and M.V. Manuel, *J. Electron. Mater.* 45, 1 (2016).
28. S.M. Kuo and K.L. Lin, *J. Electron. Mater.* 36, 1378 (2007).
29. S.M. Kuo and K.L. Lin, *J. Electron. Mater.* 37, 1611 (2008).
30. C.S. Lee and F.S. Shieu, *J. Electron. Mater.* 35, 1660 (2006).
31. Y. Cui, X.J. Liu, I. Ohnuma, R. Kainuma, H. Ohtani, and K. Ishida, *J. Alloys Compd.* 320, 234 (2001).
32. I. Ohnuma, Y. Cui, X.J. Liu, and Y. Inohana, *J. Electron. Mater.* 29, 1113 (2000).
33. H.F. Wu, M.J. Chiang, and T.H. Chuang, *J. Electron. Mater.* 33, 940 (2004).
34. H.M. Lee, S.W. Yoon, and B.-J. Lee, *J. Electron. Mater.* 27, 1161 (1998).